Mueller polarimetric imaging as a tool for detecting the effect of non-thermal plasma treatment on the skin

HANG YANG,[1,†] [ID] BO LIU,[1,†] JUNHA PARK,[2] OCÉANE BLAISE,[1] CONSTANCE DUCHESNE,[1] BRUNO HONNORAT,[1] JÉRÉMY VIZET,[2] ANTOINE ROUSSEAU,[1,3] [ID] AND ANGELO PIERANGELO[2,*] [ID]

[1]*LPP, Ecole Polytechnique, CNRS, IP Paris, Sorbonne Université, Palaiseau, 91128, France*
[2]*LPICM, Ecole Polytechnique, CNRS, IP Paris, Palaiseau, 91128, France*
[3]*antoine.rousseau@lpp.polytechnique.fr*
[†]The authors contributed equally to this work.
[*]*angelo.pierangelo@polytechnique.edu*

Abstract: Non-thermal plasma (NTP) is a promising technique studied for several medical applications such as wound healing or tumor reduction. The detection of microstructural variations in the skin is currently performed by histological methods, which are time-consuming and invasive. This study aims to show that full-field Mueller polarimetric imaging is suitable for fast and without-contact detection of skin microstructure modifications induced by plasma treatment. Defrosted pig skin is treated by NTP and analyzed by MPI within 30 minutes. NTP is shown to modify the linear phase retardance and the total depolarization. The tissue modifications are inhomogeneous and present distinct features at the center and the fringes of the plasma-treated area. According to control groups, tissue alterations are primarily caused by the local heating concomitant to plasma-skin interaction.

1. Introduction

Non-Thermal Plasma (NTP) is a weakly ionized gas produced by electric discharges and characterized by a low ionization fraction (). NTP keeps the gas temperature near room temperature, contrary to the electron temperature, which can reach more than 10^4 K [1]. In addition to the electrons, ions, and strong pulsed electric fields, NTP produced in air also generates reactive oxygen and nitrogen species (RONS) in the gas phase and the treated material [2]. Several complex biological processes appear when NTP interacts with skin tissue. The investigation of these processes opened the way to a new promising multidisciplinary research field in dermatology. Indeed, NTP can help to heal skin wounds such as burns and incisional wounds [3–5], cure skin diseases such as psoriasis [6], pruritus [7], and atopic dermatitis [8]. In clinical and preclinical trials, NTP treatment appeared to favor wound healing at low power or shorter treatment time. Indeed, NTP exhibits both antibacterial activity [9] and pro-healing effects with the stimulation of cell motility [4,10], as well as improved extracellular matrix deposition and angiogenesis in wounds [5,11].

At higher power, NTP treatment induces cell death, exhibits anti-tumoral properties [12–14], and helps blood coagulation in wounds [15,16]. These effects can also be associated with the modification and damage in the skin's extracellular matrix induced by the treatment [17,18]. However, the leading causes behind such microstructural modifications are still unclear. They may be due to the RONS but also to the increase of the skin temperature depending on the plasma treatment conditions. In particular, thermal effects can play a crucial role in NTP treatment's microstructural changes induced on the skin. Indeed, the experiments of Chernets *et al.* [19] showed that the temperature at the center of B16-F10 tumor in C57BL/6 mice is approximately

27°C higher than the average tissue temperature. The observed increase in the local temperature was associated with macroscopically visible tissue damage just after plasma exposure [19]. These macroscopic tissue modifications are due to microscopic alterations that remain very difficult to characterize and quantify.

Changes in tissue microstructure, sometimes unobservable on intensity-based images or with the naked eye, can be clearly detected by Mueller polarimetric imaging (MPI). This technique has received increasing interest in the last few years. In particular, its ability to provide a comprehensive polarimetric characterization of biological tissues at various penetration depths, using different wavelengths in the visible spectral range, is of tremendous interest for biomedical applications [20,21]. The great advantage of this technique is that it can be implemented with a wide field of view to analyze large areas (up to several cm^2) while providing information concerning the tissue microstructure, impossible to obtain with conventional intensity-based imaging. In addition, this non-invasive diagnostic tool does not require tissue contact or chemical reagents. For all these reasons, the number of biomedical applications of MPI has grown considerably in the last few years. In particular, this technique appears as a promising tool to improve cancer detection on a wide variety of biological tissues such as cervix [22–26], colon [27–29], rectum [30], intestine [31], and skin [32,33]. Recently, it has been used to characterize the photo-damaging process in mouse skin and evaluate the effectiveness of sunscreens developed to prevent skin aging and disease generated by daily UVR exposure [34]. Finally, the development of Mueller polarimetric endoscopic systems can improve the detection of pathologies on the surface of internal organs [35,36].

In this study, a 0.3~1.4 W plasma jet is used as a NTP source to treat defrosted pig skin samples. Changes in tissue microstructure were detected and quantified by means of MPI immediately after plasma treatment. As the skin samples are not in a culture medium, the focus of this study is not to reveal biological effects but to determine the predominant component of plasma (between RONS and heat) that produces changes in the tissue microstructure observed over a short time scale. Groups of pig skin samples treated with plasma under different conditions are compared to control groups, where the samples are not treated at all or are exposed only to heat or to production of H_2O_2, one of the main RONS generated by the plasma.

2. Experimental method

2.1. Plasma source, power and temperature measurement

Non-thermal plasma (NTP) is an atmospheric pressure plasma jet (APPJ), a photo of which is shown in Fig. 1(a). A schematic illustrating the operation of the APPJ in more detail is shown in Fig. 1(b). The NTP source used in this study is a glass capillary with an inner diameter of 1 mm and an outer diameter of 4 mm. The high-voltage electrode was made by surrounding the capillary with a 10 mm wide copper tape. The distance between the high-voltage electrode and the capillary outlet is 40 mm. Pure helium (5N5, Air Liquide, impurities < 5 ppm) was flowed through the capillary at 1.0 standard liter per min (SLM). The high-voltage electrode was powered by a 10 kHz AC, 16 kV peak-to-peak sinusoidal waveform. The plasma discharge propagates outside the capillary and reaches the sample located 6 mm below the capillary outlet. Figure 1(c) shows a photo of a 0.8 W plasma jet interacting with the surface of a pig skin sample. The plasma directly impacts a circular area with approximately 2 mm in diameter.

The charges carried by the plasma were measured with a 10 nF capacitor connected to the sample. During a time period of the generator, multiple plasma discharges propagated through the gas channel and reached the sample. The amount of charges ΔQ carried by one individual discharge is $\Delta Q = C\Delta U_C$ where C is the capacitance and ΔU_c is the voltage variation at the terminal of the capacitor. The average power $\bar{P}$ during one oscilloscope acquisition was measured
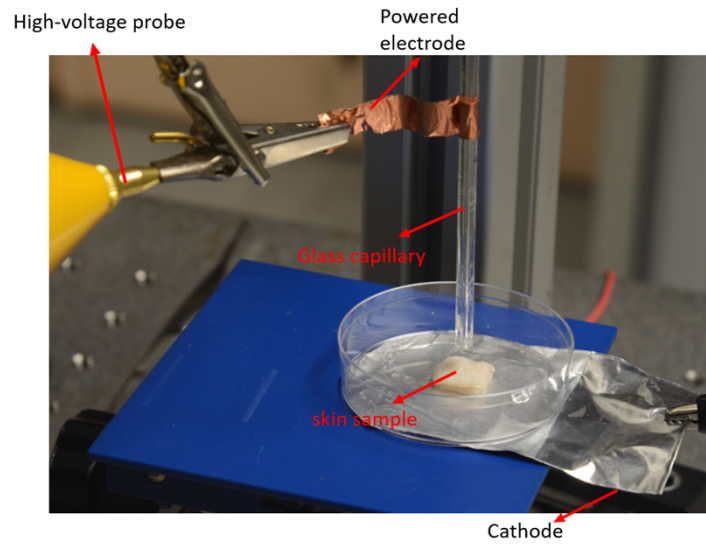
(a)
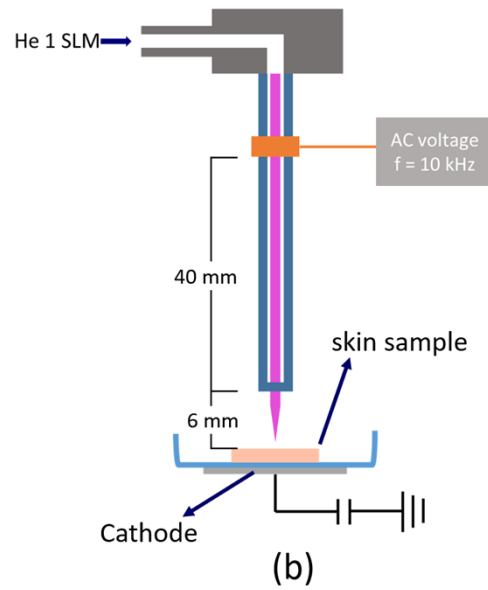
(b)
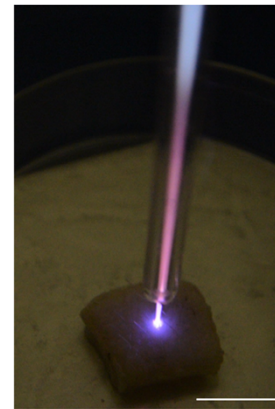
(c)

Fig. 1. (a) Photo of the homemade experimental set-up for the production of the plasma jet to treat a pig skin sample (without plasma jet). (b) Schematic of a plasma jet treating a pig skin sample. (c) Photo of a plasma jet of 0.8 W power interacting with the surface of a pig skin sample. Scale bar: 10 mm.

and calculated in real time according to:

$$\bar{P} = \frac{1}{T} \int_0^T U_s(t) \frac{dQ(t)}{dt} dt = \int_0^T U_s(t) \frac{CdU_c(t)}{dt} dt \qquad (1)$$

where T is the acquisition time of one oscilloscope measurement and U_s is the voltage applied at the high-voltage electrode. U_s was measured using a high-voltage probe 1000× attenuation (Teledyne Lecroy PPE 20 kV). U_c was measured using a low-voltage passive probe 10× attenuation (Teledyne Lecroy PP08). The probe voltages were acquired and registered using an oscilloscope (Teledyne Lecroy Waverunner 625Zi, bandwidth = 2.5 GHz). The plasma power was varied between 0.3 W and 1.5 W and controlled by modifying the peak-to-peak amplitude of U_s.

The plasma discharge increases the temperature of the treated area. The temperature of this area was measured with an infrared camera (TESTO 868, Lenzkirch, Germany). The reported temperature refers to the maximum temperature measured in the center of the treated area. The final steady state temperature was found to be dependent on the plasma power. It reached 45°C, 55°C, 63°C, and 73°C with a plasma jet of 0.5 W, 0.8 W, 1.0 W, and 1.4 W power, respectively. More details on skin temperature changes during plasma treatment are shown in Fig. S1 and Fig. S2 (Supplement 1).

2.2. Ex-vivo sample preparation and group description

In this work, defrosted pig skin samples were used as the skin model to ensure the reproducibility of the experiments. These samples were collected from a sacrificial pig (Large White, female, 8 weeks old, about 40 kg) used for research purposes and with strictly controlled characteristics. We cut a large piece of skin from which several square samples of approximately the same size (1.5 cm × 1.5 cm) were obtained. The initial piece was very uniform in thickness and did not contain fat. The samples thus obtained were characterized by a very similar thickness and composition. A depilatory cream was applied to remove the hair. Then they were stored in a sealed box at -20°C for freezing in order to preserve their properties over months and defrosted at the time of the experiments which were performed with the same protocol described in detail later in the text. As the *ex-vivo* defrosted skin samples are dead material, no biological or metabolic effects were expected. The experiments were performed between February 2021 and March 2022.

The treatment and measurement protocol are summarized in Fig. 2. First, each skin sample was taken out of the refrigerator and its mass m_0 was measured using an analytical balance with a precision of 0.1 mg. Right after, the "dry" sample was imaged using MPI. Then, it was soaked in Phosphate Buffered Saline solution (PBS 1×) for 20 min to set its temperature and moisture. Measurement of the mass m_s and MPI of each soaked sample were performed immediately afterward.
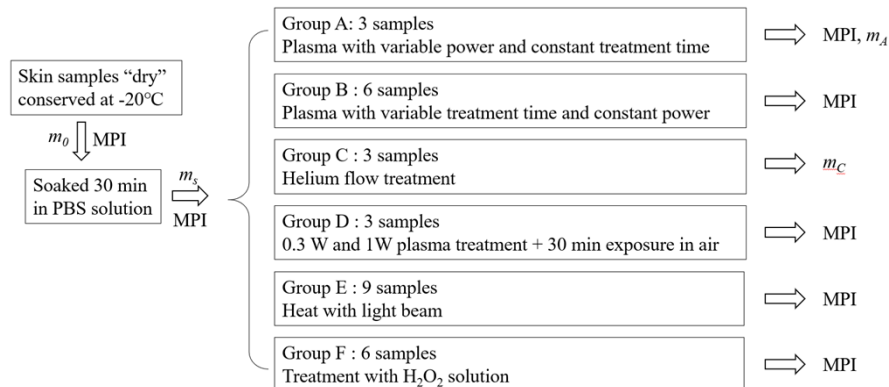

Fig. 2. Summary of the experimental protocol, including plasma treatment, mass measurements, and Mueller Polarimetric Imaging (MPI).

All analyzed samples were divided into six groups, indicated by letters from A to F. Each sample was treated in a maximum of four different locations. After all treatments, mass measurement and MPI were performed again. For all plasma treatments mentioned below, the distance of the capillary outlet from the skin surface is 6 mm and the helium flow rate is 1 standard liter per minute (SLM).

A. The samples in Group A ($n = 3$) were treated with plasma at variable power and constant treatment time. On each sample, four different locations were irradiated for 4 minutes at 0.5 W, 0.8 W, 1 W, and 1.4 W, respectively.

B. The samples in Group B ($n = 6$) were treated with plasma at constant power and variable treatment time. In particular, 3 samples were treated with 1 W plasma jet for 0.5 min, 1 min and 1.5 min in three different locations. In the same way, the other 3 samples were treated with 1 W plasma jet for 2 min, 4 min, and 6 min in three different locations.

C. The effect of the gas flow alone was investigated for the samples of Group C ($n = 3$). These samples were placed under the capillary with 1.0SLM helium flow without any applied voltage. In these conditions, no plasma was formed. The exposure time (4 min) and the distance between the capillary and the skin (6 mm) were similar to those used for the experiments performed on the samples of Group A. Group C permits to control the water loss in the samples and determine the polarimetric effects it could induce.

D. In Group D ($n = 3$), each sample was treated in two different locations at 0.3 W and 1 W, respectively, for 4 min. Skin modifications were investigated 5 and 30 minutes after irradiation to determine whether a delayed or progressive treatment effect occurred.

E. The effect of heating was explored in Group E ($n = 9$). The samples were illuminated with light from a halogen lamp (Olympus CLH-CS) for 4 minutes. Two convex lenses were used for focusing the light beam on the sample surface in order to illuminate a circular area of 2 mm in diameter, close to that irradiated by the plasma jet. The focused beam increased the local temperature to 43°C, 56°C, and 65°C, depending on the chosen intensity of the light source. Thus, the maximum skin temperatures obtained in Group E are close to those induced by plasma-skin interaction under the different conditions considered.

F. The effect of H_2O_2 exposure was investigated only for samples within Group F ($n = 6$). Indeed, H_2O_2 is the main reactive species produced by the plasma discharge. In Groupe F, a 5.0 μL droplet of 0.2%v H_2O_2 solution was deposited on the pig skin surface using a micropipette. The concentration of the H_2O_2 solution was determined through an experiment described in section 2.3. The droplet on the surface of the sample covers a circular area with approximately 2 mm diameter. The total amount of H_2O_2 in the droplet was 293 nmol, similar to that produced by the plasma jet. Three samples were exposed for 4 min and three others samples for 1 hour in only one location.

2.3. *H_2O_2 quantification*

H_2O_2 in APPJs is mostly formed within the plasma jet and is transported to targets like liquid or skin samples [37]. The production of H_2O_2 depends on many factors such as the geometry of the plasma jet and the flow rate. Thus, the production of H_2O_2 has to be characterized specifically for each system.

In this study, the concentration of H_2O_2 solution used for Group F was determined by a simple experiment. In particular, 5 mL of distilled water was exposed to a 1 W plasma jet for 4 min. The capillary exit was placed at a distance of 6 mm from the irradiated surface of the liquid sample. The total amount of H_2O_2 was measured with the photometric method described hereafter. About

0.9 mL of plasma-activated water was added to a cuvette. A reagent containing copper(II) ions (Sigma-Aldrich 1.18789) was added to the cuvette containing the liquid sample, in which the H_2O_2 reduces the copper(II) ions to copper(I) ions and forms an orange colored complex. After 15 min incubation, the absorption was measured at 433 nm with a photometer (Secomam Uviline 9100).

The result showed that the concentration of H_2O_2 in the plasma-activated water was 58.5 μM. Thus, the total amount of H_2O_2 produced in the 5 mL water was 293 nmol. As shown n Fig. 1(c), the plasma directly impacts a circular area with a diameter of approximately 2 mm, which can be covered by a droplet of water of 5 μL. Supposing the 293 nmol H_2O_2 is 100% transported to the skin sample, the 5 μL solution should contain 293 nmol H_2O_2, corresponding to a volume concentration of approximately 0.2%.

2.4. Muller polarimetric imaging (MPI)

The skin samples were analyzed using an in-house sequential full-field Mueller polarimetric imager (MPI) in backscattering configuration [38]. In this system incoherent white light is delivered by a 150 W halogen source (Olympus CLH-CS) and transported to the optical bench using a liquid light guide (Thorlabs LLG0528-6). A collimator, placed at the output end of the liquid light guide, is used to produce a light beam with a spot size of 6 cm in diameter at a distance of about 20 cm (from the collimator) corresponding to the position of the sample to be analyzed. In particular, the sample is positioned in the middle of the beam where the maximum light power of about 7.5 mW is measured by a power meter (MELLES Griot 13PEM001).

The light flux increases the local temperature of the skin sample from $21.7 \pm 0.4°C$ (room temperature) to $22 \pm 0.4°C$ after 10 minutes exposure, while the measurement time using the MPI is less than 1 minute. Therefore, the effect of such low heating on the sample can be neglected, as shown in Fig. S3 (Supplement 1).

A Polarization State Generator (PSG), placed right after the collimator, temporally modulates the polarization of the light illuminating the sample. Four independent polarization states, described by four Stokes vectors, are produced sequentially. These four Stokes vectors are grouped as the columns of a 4×4 real-valued modulation matrix called W. The light reflected by the sample is analyzed with a Polarization State Analyzer (PSA) placed in front of the detector. After interacting with the sample, each polarization state generated by the PSG is analyzed through four independent polarization configurations of the PSA, which are described by four Stokes vectors, grouped as the rows of a 4×4 real-valued analysis matrix called A. The described measurement protocol provides 16 intensity images that are stacked in a 4×4 real-valued matrix **B** given by:

$$\mathbf{B} = \mathbf{AMW} \tag{2}$$

where **M** is the Mueller matrix of the sample allowing its comprehensive polarimetric characterization. After determining the **W** and **A** matrices through a calibration process [39], **M** can be obtained from Eq. (2) using the following expression:

$$\mathbf{M} = \mathbf{A^{-1}BW^{-1}} \tag{3}$$

The PSG and PSA have been constructed using ferroelectric liquid crystals [40,41]. A monochromatic CCD camera (f080b Allied Vision, 512×386 pixels, 14 bits) is used as a detector. A zoom lens (Optem FUSION 12.5:1), characterized by a working distance of 38 cm, is placed in front of the CCD camera for adjusting the field of view to the sample size. In particular, a field of view of 5×4 cm^2 was considered for the experiments performed in this study. The actual measured resolution of the imaging system was about 150 μm/pixel. A dichroic filter (Thorlabs FB550-40, 40 nm FWHM) was placed in front of the CCD camera to acquire images at 550 nm with a spectral bandwidth of 40 nm. The light penetration depth is of the order of a few hundred micrometers for this wavelength.

The main polarimetric properties of the sample were obtained from **M** using the Lu-Chipman decomposition [42]. This decomposition allows expressing **M** using the following expression:

$$\mathbf{M} = \mathbf{M}_\Delta \mathbf{M}_R \mathbf{M}_D \qquad (4)$$

where $\mathbf{M}_\Delta$, $\mathbf{M}_R$ and $\mathbf{M}_D$ are the Mueller matrices of a depolarizer, a birefringent medium, and a diattenuator, respectively. The most relevant polarimetric properties for the skin are the total depolarization (Δ) and the linear phase retardance (LR). The parameter Δ quantifies the ability of the sample to depolarize both linear and circular polarization states. It is defined as:

$$\Delta = 1 - \frac{|a| + |b| + |c|}{3} \qquad (5)$$

where the coefficients a, b and c are the eigenvalues of $\mathbf{M}_\Delta$. In Eq. (4), $\Delta = 0$ for a non-depolarizing sample and $\Delta = 1$ for a pure depolarizing sample.

The parameter LR quantifies the difference in optical phase shifts between two main orthogonal polarization eigenstates. It is defined as:

$$LR = \arccos\left(\frac{tr(\mathbf{M}_R)}{2} - 1\right) \qquad (6)$$

where $tr(\mathbf{M}_R)$ is the trace of $\mathbf{M}_R$. In general, LR varies between 0° and 180° for biological tissues.

The relevance of other polarimetric parameters such as the azimuth of the slow axis of linear retardance and the total diattenuation was also evaluated. However, these parameters did not exhibit significant effects after the plasma treatment, as shown in Fig. S4 (Supplement 1).

2.5. Statistical analysis

Statistical analysis was performed using Prism software (GraphPad Software, San Diego, CA). The measured value for mass, linear phase retardance, and/or total depolarization, was compared between two groups with a parametric paired t-test.

A one-way parametric ANOVA (Analysis of Variance) was used to compare more than two groups. The analysis was corrected for multiple comparisons using Dunett's statistical hypothesis test.

Each test provided a *p*-value that allowed the statistical significance of the results to be assessed. The null hypothesis is rejected if $p < 0.05$. It means that the difference between two groups should be considered statistically significant. In particular, the *p*-values obtained in this study were indicated as "*", "**", and "***", if they were lower than 0.05, 0.01, and 0.001, respectively. If $p > 0.05$, the null hypothesis cannot be rejected. It means that the difference between two groups should be considered statistically non-significant (denoted as "ns" in the following text).

3. Results

3.1. Effect of soaking and drying on polarimetric properties

Since *ex-vivo* skin samples can dry out very quickly, it was essential to quantify the water loss during the experiments and assess its effect on the measurement of LR and Δ. The mass of a sample after treatment is denoted as m_A for group A and as m_C for group C. As a reminder, the mass of "dry" sample taken out of the refrigerator is indicated as m_0, while the mass of a sample after soaking is denoted as m_s, as explained above.

Figure 3 shows the measured value for mass compared between different groups. In particular, m_s, m_A, and m_C are normalized to m_0 for each sample.

The mass of the soaked samples increased on average by about 10% compared to that of dry samples ($p < 0.001$). The comparison between the group of soaked samples and Group C shows
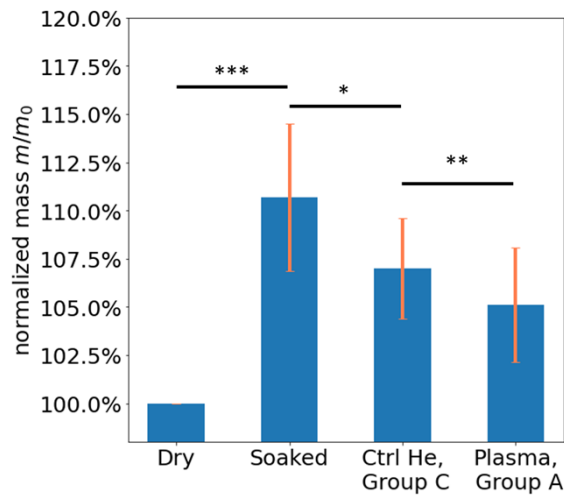
Fig. 3. Normalized mass of soaked, group C (control He flow only), and plasma Group A. The mass was normalized to the initial mass of the sample m_0 (dried). Treatment time: 4 min.

that about 3% of the mass loss is due to drying caused by the helium flow alone ($p<0.05$), which is always present during plasma treatment. Furthermore, the comparison between Group C and Group A shows that plasma treatment alone contributes to an additional 3% mass loss ($p<0.01$).

In a first step, the linear retardance LR and the total depolarization Δ were averaged over all pixels in a region of interest (ROI) selected for each sample.

Then, the mean and the standard deviation of the mean values obtained for LR and Δ in the first step, within the ROI selected for each sample, were calculated for all samples treated under the same conditions.

Figure 4(a) compares, as an example, the M11 unpolarized intensity images (I – II), as well as the LR images (III – IV) and Δ images (V – VI), for a representative skin sample before and after soaking. The ROI selected in the central area of the skin sample is marked by a white circle in Fig. 3(a)-(I). The edges of the skin sample were excluded from the ROI as they undergo accelerated drying compared to the central area. Figure 4(b) shows the statistical comparison of LR between the group of dry skin samples and the group of soaked skin samples. Soaking significantly decreased LR ($p<0.05$) by about 16%. The change in total depolarization Δ caused by soaking is not shown because it is non-significant ($p>0.05$).

3.2. Modification of LR due to plasma treatment

Figure 5(a) shows the M11 unpolarized intensity images (I – IV), as well as LR images (V – VIII) and Δ images (IX – XII) of a skin sample treated over 4 minutes at locations L1 and L2 with a plasma jet of 0.3 W and 1 W, respectively (Group D). The treatment locations are marked with white circles in Fig. 5(a)-II. The maximum temperature, measured using the infrared camera, reached 35°C and 63°C in L1 and L2 locations, respectively. MPI was performed before the plasma treatment, then 5 min and 30 min afterwards.

The fourth column of Fig. 5(a), shows the area in the dotted red square of Fig. 5(a) III zoomed by a factor of 3. Precisely Fig. 5(a) IV, Fig. 5(a) VIII, and Fig. 5(a) XII show the zoomed images of M11, LR, and Δ, respectively. No notable changes were observed in the M11 unpolarized intensity images for location L1. Nevertheless, at location L2, the M11 unpolarized intensity images show that the central part of the treated area becomes darker and smoother after treatment, as shown in Fig. 5(a) IV. In addition, no notable changes in LR and Δ were observed in L1,
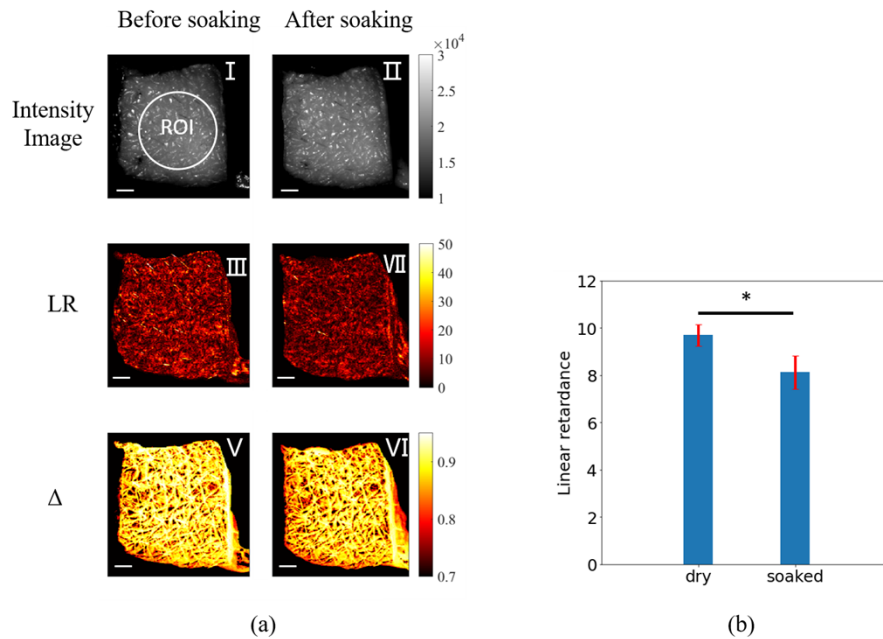
Fig. 4. MPI before and after soaking (Group D). (a) Intensity-based, linear retardance LR, and Δ image of the pig skin. (b) Average LR of 3 pig skin samples before and after soaking. Scale bars in (a): 2 mm.

treated with lower power plasma. In contrast, 1 W plasma treatment in L2 produced observable changes in LR and Δ within a circular area, as shown in Fig. 5(a) VIII and XII, respectively.

Two different zones, delimited by two concentric circles, can be clearly observed for LR and Δ parameters. In particular, the innermost circle enables to delimit the central area, which is different for both parameters compared to the surrounding ring area. As the spatial pattern produced by the plasma treatment was not perfectly identical for LR and Δ, the diameters of the concentric circles were selected independently for these two parameters, as shown in Table 1.

Table 1. Diameter of the circles delimiting the center and ring area for LR and Δ. Groupe D (n = 3)

Diameter ± SD	Innermost circle	Outermost circle
LR	1.8 ± 0.9 *mm*	3.7 ± 0.7 *mm*
Δ	1.2 ± 0.6 *mm*	2.3 ± 0.8 *mm*

The diameter of the innermost circle is 44% smaller for Δ than LR. Similarly, the diameter of the outermost circle is 48% smaller for Δ than for LR.

The central circle selects an area where LR is significantly lower compared to the surrounding ring area after plasma treatment, as shown in Fig. 5(a) VIII. On the other hand, the ring selects an area where LR after treatment is significantly higher compared to the untreated area. Figure 5(b) shows quantitatively that after plasma treatment, the LR in the ring area is significantly higher than the LR in the central area ($p < 0.001$).

The value of Δ decreases within the selected ring, compared to the untreated skin, as shown in Fig. 5(a) XII. The central circle selects a region where Δ is more homogeneous than in untreated skin and higher than in the area contained within the surrounding ring. Figure 5(c) shows
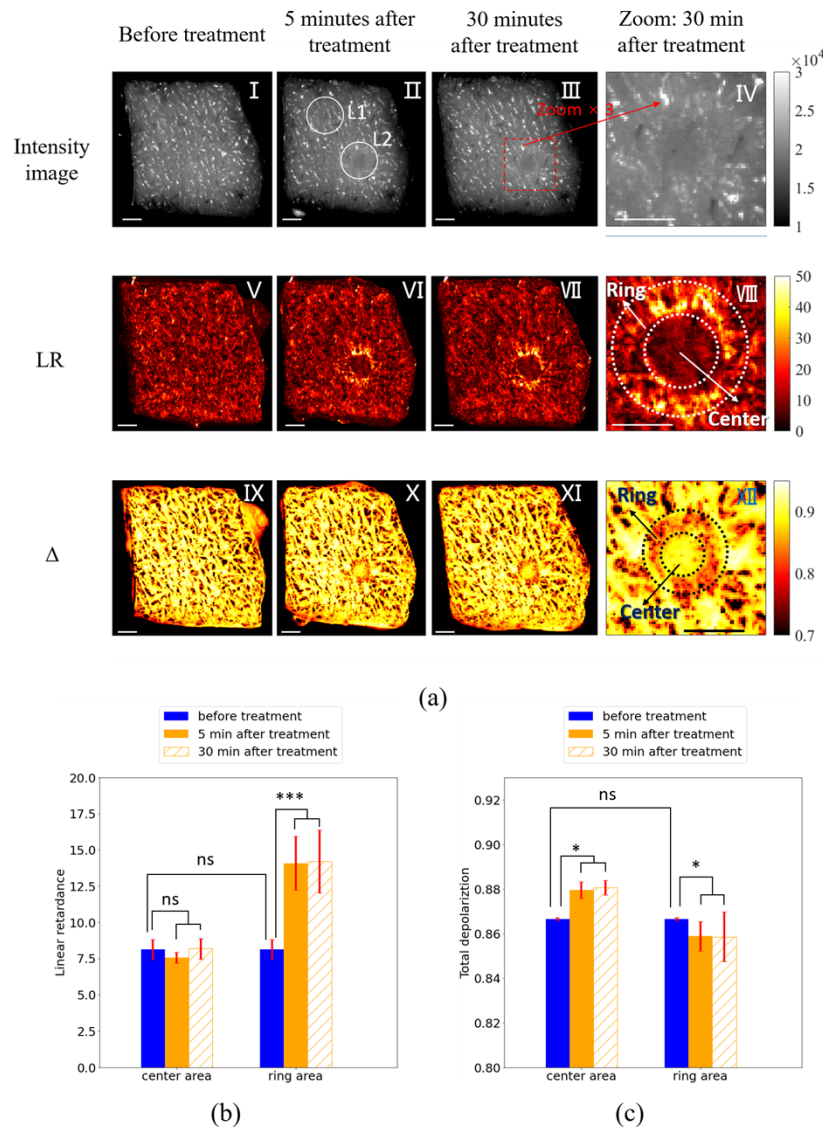
Fig. 5. MPI of Group D samples. (a) Intensity image, linear retardance (LR), and total depolarization (Δ) of a skin sample before treatment, 5 and 30 min after treatment. Locations L1 and L2, marked with white circles in II, were treated with 0.3 W and 1 W plasma, respectively, for 4 min. The skin reached a maximum temperature of 35°C and 63°C for locations L1 and L2, respectively. The fourth column of (a), shows the area in the dotted red square of (a) III zoomed by a factor of 3. Precisely (a) IV, (a) VIII, and (a) XII show the zoomed images of M11, LR, and Δ, respectively. (a) VIII and XII shows how the central and ring areas area selected. (b) The average linear retardance in the center and ring areas before and after treatment. (c) The average total depolarization in the center and ring areas before and after treatment. Scale bars in (a): 2 mm.

quantitatively that after plasma treatment, the Δ value in the selected ring area is significantly lower than in the central area and in the untreated area ($p<0.05$).

For group D, Δ seems to slightly increase after plasma treatment compared to before treatment as shown in Fig. 5(c). However, in this case, it is difficult to verify whether this difference

is significant by having a *p*-value close to 0.05 (*p* = 0.048). Nevertheless, considering all 12 samples of groups A, B and D, it was observed that the increase of Δ in the central area due to plasma treatment is in most cases negligible compared to the untreated area (*p*>0.05).

The LR and Δ images acquired 5 and 30 minutes after treatment did not show visible differences, as can be seen in Fig. 5(a). The average value of LR and Δ was calculated for the ring and the central area in location L2. Between 5 min and 30 min, the difference in LR and Δ is non-significant (*p*>0.05) for both the central area and the ring area, as shown in Fig. 5(b) and Fig. 5(c). These results prove that all the modifications observable with MPI occur instantly after treatment. In particular, the slight drying of the skin or possible delayed/gradual effects of plasma treatment do not contribute to the changes in polarimetric properties.

Finally, it should be noted that the changes in linear phase retardance previously described for soaking is minor compared to those caused by plasma treatment.

3.3. Effect of plasma power on LR and Δ

Figure 6 shows the MPI of a pig skin sample treated in locations L1, L2, L3, and L4 at 0.5 W, 0.8 W, 1 W, and 1.4 W, respectively, for 4 minutes each (group A). The unpolarized M11 intensity image in Fig. 6 (I – II) shows that the central part of the treated area became darker at locations L2, L3 and L4, while it remained unchanged at location L1 treated by 0.5 W plasma. Moreover, the 0.5 W plasma treatment produced no noticeable changes in LR and Δ images, as shown in Fig. 6 (III – IV) and Fig. 6 (V – VI), respectively. In contrast, MPI showed that the plasma effect became more evident and affected a larger area with increasing the treatment power.
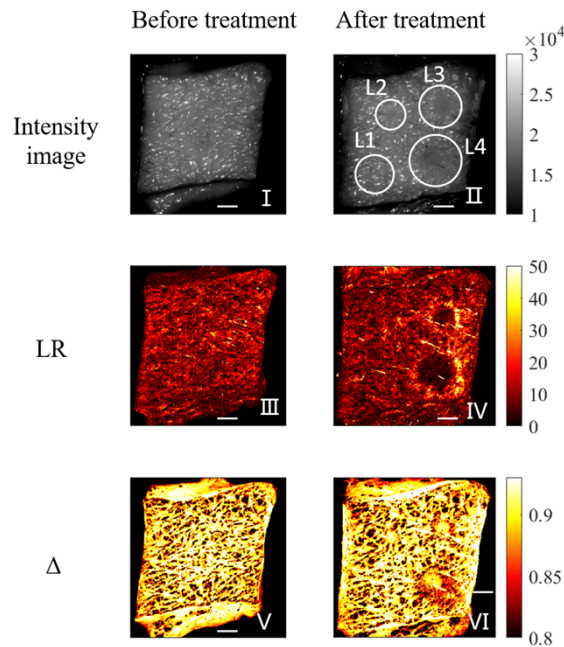

Fig. 6. Variable plasma power and constant treatment time (Group A). Intensity-based image, linear retardance (LR), total depolarization(Δ) of a representative skin sample before and after plasma treatment. The plasma power was 0.5, 0.8, 1.0, and 1.4 W for locations L1, L2, L3, and L4, respectively. The treatment time was 4 min. Scale bars: 2 mm.

Figure 7(a) shows the area bounded by the central circle for LR as a function of plasma power. In particular, the plasma power is expressed as a function of the maximum temperature reached by the skin in the treated zone. Indeed, the maximum temperatures of 45°C, 55°C, 63°C and
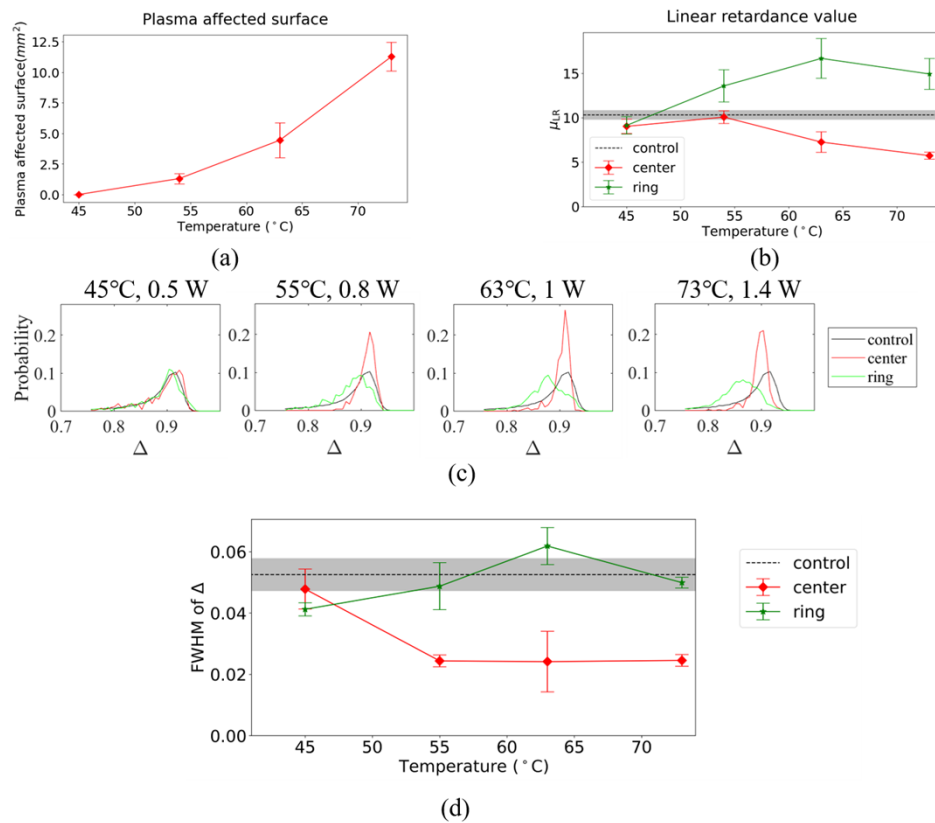
Fig. 7. Variable plasma power and constant treatment time (Group A). Treatment time: 4 min. The plasma power was 0.5, 0.8, 1.0, and 1.4 W leading to the maximum final temperature of 45, 55, 63, and 73 °C. (a) Area of the "center area" for LR in mm^2. (b) Average LR in the center, ring, and control area (untreated skin). (c) Probability distribution of the pixels according to Δ for a representative skin sample. (d) Average FWHM of the Δ probability distribution as a function of the maximum temperature reached. The error bars are the standard deviation on all the samples treated with a given power ($n = 3$). The value of the control is measured before the treatment and is indicated with black dash line. The standard deviation is shown with the gray area.

73°C, correspond to power levels of 0.5 W, 0.8 W, 1.0 W and 1.4 W, respectively. The central area, where LR is lower than the surrounding ring area, increased monotonously with increasing plasma power, becoming larger than the area of tissue actually in contact with the plasma jet (about 2 mm^2).

Figure 7(b) shows the evolution of the mean value μ_{LR} of LR as a function of temperature in the central and annular region. The "control" curve represents μ_{LR} for the untreated skin. This parameter significantly decreased in the central area compared to untreated skin as the power was increased from 0.5 W (45°C) to 1.4 W (73°C). Similarly, it significantly increased in the ring area with increasing power. The ANOVA test showed that the decrease in the central area of LR with power is statistically significant ($p<0.01$). Similarly, the increase of LR in the ring area with power is also statistically significant ($p<0.0001$).

The mean value μ_Δ of Δ (not shown) did not change significantly (p > 0.05) in the central area. In the peripheral area, it seemed to decrease slightly. However, this decrease is also not significant (p > 0.05). However, the probability distribution shape of Δ visibly changed between

central and ring areas, as well as between them and the untreated part, as shown in Fig. 8(c). Indeed, the distribution of Δ in the central area becomes narrower with increasing plasma power. Moreover, it varies, although more slightly, also within the ring area. Figure 7(d) shows the evolution of the full width at half maximum (FWHM) for the probability distribution of Δ as a function of maximum temperature after plasma treatment both for the central area and the ring surrounding area. In the central area, the FWHM decreases significantly ($p<0.001$), showing that Δ becomes more spatially homogeneous. On the contrary, the variation of the FWHM within the annular zone is non-significant ($p>0.05$).

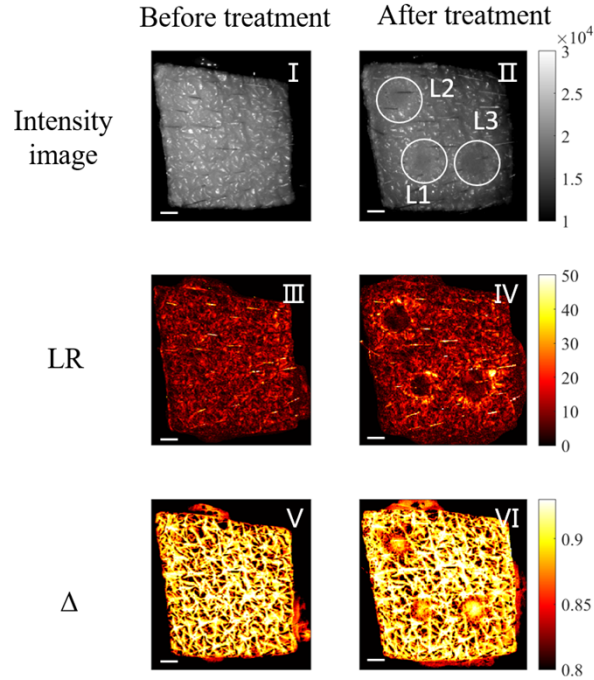**Fig. 8.** Variable plasma treatment time for constant power (Group B). Intensity-based image, linear retardance (LR), total depolarization(Δ) of a skin sample before and after treatment. The treatment time was 2, 4, and 6 min for locations L1, L2, and L3, respectively. The plasma power was 1 W. The surface reached a maximum temperature of 63°C at each location. Scale bars: 1 mm.

3.4. Effect of plasma treatment time on LR and Δ

The effect of plasma treatment time was investigated in the range 30 s ~ 6 min, with constant plasma power of 1 W (Group B). The pig skin reached a maximum temperature of 63°C.

Figure 8 shows M11 unpolarized intensity images (I – II), as well as LR images (III – IV) and Δ images (V – VI) of a representative sample treated for 2, 4, and 6 min in the areas indicated as L1, L2, and L3, respectively. As before, the M11 unpolarized intensity images showed that the central part of treated area became darker and smoother at locations L1, L2 and L3. The LR and Δ images show that the extension of the area modified by the irradiation becomes more prominent with increasing treatment time.

Figure 9(a) shows that the area contained in the central circle increased monotonously with treatment time, becoming larger than the area actually in contact with the plasma jet (about 2 mm^2).
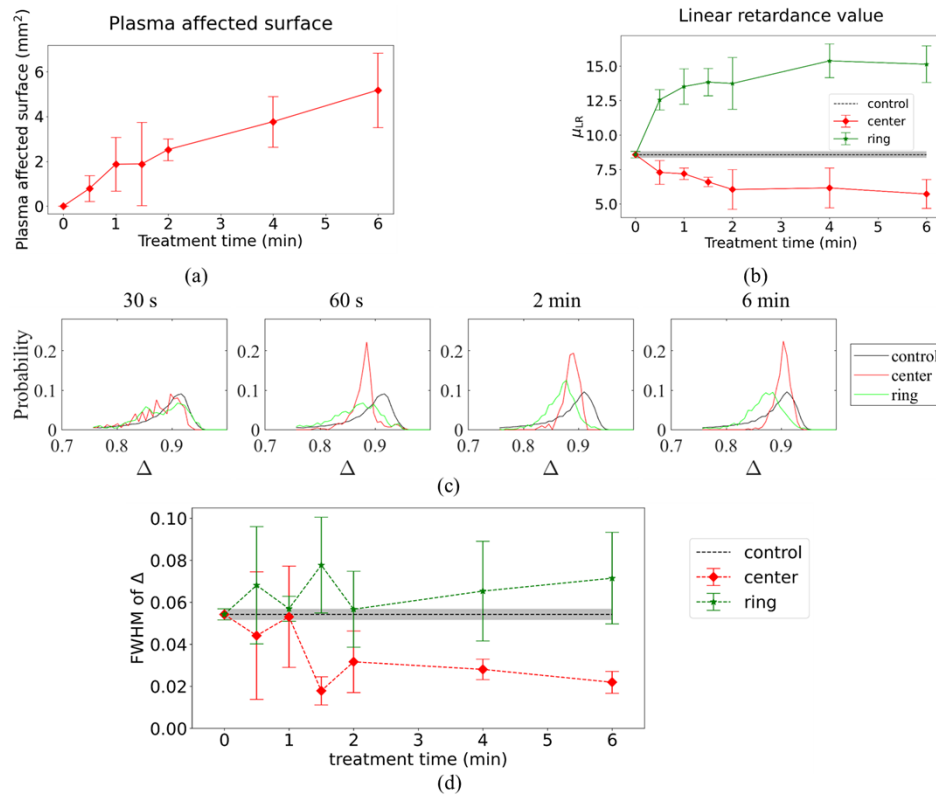
Fig. 9. Variable plasma treatment time for constant power (Group B). (a) area of the "center area" for LR. (b) Average value of LR in the center, ring, and control area (untreated skin) as a function of the treatment time. (c) Probability distribution of the pixels according to Δ for a representative skin sample. (d) Average FWHM of the Δ probability distribution as a function of the treatment time. The error bars are the standard deviation on all the samples treated for a given time ($n = 3$). The plasma power was 1 W. The surface reached a maximum temperature of 63°C at each location. The value of the control is measured before the treatment and is indicated with black dash line. The standard deviation is shown with the gray area.

Figure 9(b) shows that the mean value μ_{LR} of LR increased for the ring and decreased for the central circle with increasing treatment time. However, the greater change in LR occurred before 2 min. Indeed, the LR remained quite stable after 2 min, within the limits of the error bars. The ANOVA test showed that the effect of treatment time on LR is statistically significant both for the central area ($p<0.05$) and for the ring area ($p<0.001$).

The change in the mean value μ_{Δ} of Δ (not shown) was non-significant ($p>0.05$) for the central and ring area. However, also in this case, the probability distribution shape of Δ visibly changed between central and ring area, as well as between them and the untreated skin. Figure 9(c) shows that the distribution of Δ in the central zone becomes narrower with increasing treatment time. Moreover, it changes, although more slightly, in the ring area.

Figure 9(d) shows the evolution of the FWHM for the probability distribution of Δ as a function of treatment time both for the central area and the ring surrounding area. In the central area, the FWHM decreases significantly ($p<0.05$), showing that Δ becomes more spatially homogeneous. In particular, the FWHM strongly decreases up 2 min, whereas it remains relatively constant

over a longer treatment time. On the contrary, the modification of the FWHM in the ring area is non-significant ($p>0.05$).

3.5. Heating is the main contribution to the observed changes in MPI compared to H_2O_2 local effect

Two experiments were performed to elucidate the effect of temperature and H_2O_2 on the polarimetric properties of pig skin. Indeed, the exposure to plasma irradiation generates heat and H_2O_2 in the skin.

The pig skin samples were heated by a light beam for 4 min to investigate the temperature role on the tissue modifications (Group E). The focused light beam increased the local temperature to 43°C, 56°C, and 65°C, reproducing the thermal conditions observed in Group A (variable power and constant treatment time) using 0.8 W, 1.0 W, and 1.4 W plasma jet, respectively.

The intensity of the light spot, shown in Fig. 10(a), was measured as a function of the distance to the beam center by placing a CCD-camera (Stingray F-080 with Sony ICX204) at the location of the skin sample. The FWHM of the light distribution was close to the diameter of the plasma-treated surface.
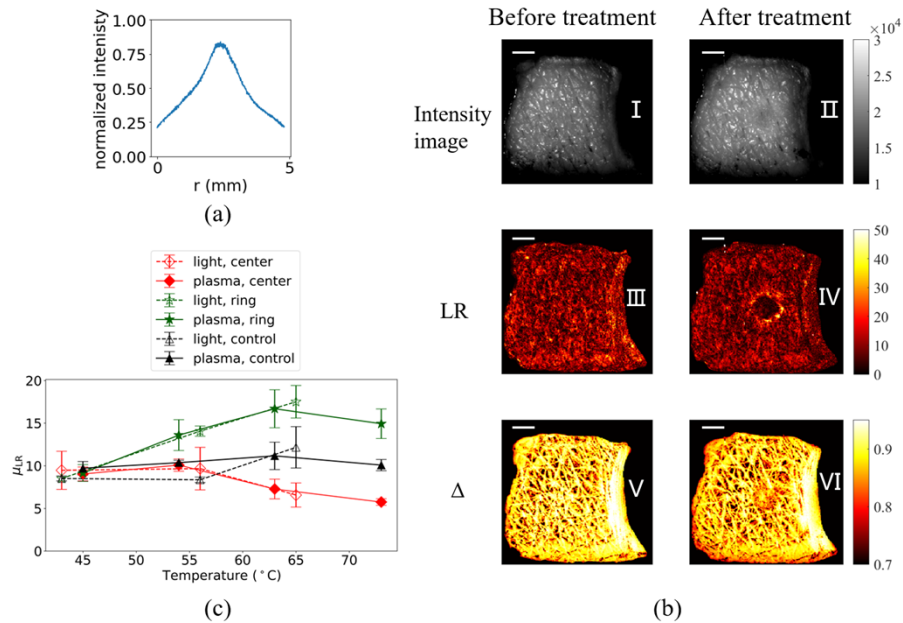

Fig. 10. Group E. (a) shows the light intensity of the focused light beam on the sensor. The light intensity is measured along a straight line that goes across the center of the circular light spot. (b) show the intensity image, LR and Δ of a skin sample before and after treatment. It is treated in the center by the focused light beam, which heats the surface to 63°C. (c) shows the curve of LR mean value in the center(red) and ring area(green) of skin samples treated by light (dash lines) or by plasma (solid lines). The black curves represent the LR of the corresponding area before treatment.

Figure 10(b) shows the M11 unpolarized intensity images (I – II), as well as the LR images (III – IV) and Δ images (V – VI) of a representative skin sample before and after being heated to 65°C. As before, the M11 unpolarized intensity images show that the central part of treated area became darker and smoother. In addition, the focused light beam produced observable changes in LR and Δ within a circular area, as shown in Fig. 10(b) IV and VI, respectively.

In particular, the spatial patterns in LR and Δ images produced by the focused light beam are similar to those produced by the plasma treatment in different conditions. Indeed, also in this case, two different zones, delimited by two concentric circles, were clearly observed in LR and Δ images.

The average values of LR were measured in the central area and in the surrounding ring area. Figure 10(c) shows the evolution of the mean value μ_{LR} of LR as a function of temperature for the light-treated (dotted lines) and plasma-treated (solid lines) skin. No significant difference was observed for these two groups ($p>0.05$) both for central and surrounding ring area. This result suggests that the thermal component of plasma treatment plays a predominant role in modifying the polarimetric properties of pig skin.

Finally, the pig skin samples were exposed to H_2O_2 (0.02%v) droplets for 4 min and 1 h (Groupe F). This experiment was conducted to determine whether the main RONS produced by the plasma, in particular H_2O_2, could also affect the polarimetric properties of the skin. The MPI revealed that no noticeable effects can be observed. Thus, the amount of H_2O_2 produced by the plasma jet does not affect the polarimetric properties of the skin.

4. Discussion

The main objective of this study is to demonstrate the strong potential of full-field Mueller polarimetric imaging (MPI) to detect and quantify short-term skin damages generated by non-thermal plasma treatment (NTP) and to determine the main component (between heat and RONS) that produces the observed tissue changes.

This study showed that plasma treatment generates a strong modification of LR and Δ. The measurement of LR and Δ is strongly affected by the signal-to-noise ratio (SNR). Specifically, if the SNR is low, i.e., for poorly illuminated pixels for which the measured unpolarized light intensity (determined by the unnormalized coefficient M11 of the measured Mueller matrix) is less than 500 ADUs, the determination of LR and Δ may be characterized by very high uncertainties especially if the B matrix is acquired only once. In this case, in order to optimize the SNR and significantly reduce the measurement uncertainty for both parameters of interest, the B matrix has to be acquired and averaged a large number of times, which significantly increases the measurement duration.

For the experiments described in this study, the illumination was optimized by taking great care not to saturate the CCD camera image. Under these illumination conditions, almost all pixels contained in a region of interest for a given sample were characterized by light intensity well above 500 ADUs. In addition, the intensity matrix B was acquired and averaged 16 times. In this way, the SNR was optimized, allowing the determination of the LR and Δ parameters with less than 0.5% and 1° error, respectively. The acquisition time is less than 1 minute, which limits artifacts in the images due to natural deformations of the samples analyzed ex vivo during the measurements.

Two different areas, delimited by two concentric circles, can be clearly observed in the LR and Δ images. In particular, the innermost circle delimits a central area characterized by a significantly lower LR value compared to the surrounding annular area and the untreated tissue. The central zone is also characterized by a strong increase in temperature. Furthermore, in the central zone, the temperature increases with increasing plasma power. Indeed, by varying the plasma power from 0.5 W to 1.4 W, the skin temperature increases from 45°C to 73°C; (4 min being the treatment time for each chosen plasma power). Furthermore, the diameter of this central area also increases with plasma power (hence with temperature) and can reach a larger diameter than the region directly irradiated by the plasma jet (about 2 mm).

This effect suggests that the thermal energy produced in the directly irradiated region is transferred to the surrounding zones, leading to a strong increase in their temperature, a modification of their microstructure and an expansion of the circular central zone, as observed.

At the same time, the increase of temperature in the central zone also produces a decrease of LR. Denaturation of collagen is a possible effect caused by heating above 45°C [43,44]. This process should decrease the local organization of the fibers, which could explain the observed decrease in LR. In addition, a radial temperature gradient is created from the central area to the more distant surrounding area. In particular, the zone furthest from the central zone remains at the ambient temperature (about 22°C). The annular zone represents the transition between the highly heated central zone and the unheated surrounding zone which remains at room temperature. The tissue can shrink in the central zone under the effect of the heat while the unheated zone remains unchanged. Thus, the fibers in the transition ring area can be mechanically pulled towards the circularly symmetric central area. This mechanical pulling process should lead to a reorganization of the fibers in the ring zone with a local increase in their density, which could explain the observed increase in LR.

On the other hand, the Δ image also shows a central circular area that becomes more and more homogeneous (without significant change in its mean value) with increasing power. This area is surrounded, by an annular area where a slight decrease in depolarization is found. The spatial pattern observed for Δ is very similar to that observed for LR. However, the diameter of the central zone and the annular zone of Δ are smaller than those observed for LR. The interpretation of the observed depolarization effects remains rather difficult and cannot be directly related to the effects observed for LR. Furthermore, although the considerations made for LR are quite reasonable, they remain qualitative as we do not have a direct demonstration of the process described. It is clear that MPI is very effective in detecting microstructural changes in skin tissue after plasma treatment by measuring several polarimetric parameters. However, the interpretation of the results obtained may be difficult without the availability of a relevant model that allows associating to a certain macroscopic polarimetric response the corresponding microscopic structure. For the interpretation of the results obtained with the MPI, the coupling of this technique with another imaging technique able to provide a direct observation of the microstructure of the analyzed tissue is crucial. For instance, coupling of MPI with PS-OCT may be a very promising strategy for the interpretation of the results and the development of a relevant model, which will be one of our goals for the future [45,46].

In support to the above hypothesis that thermal effects play a key role in altering the observed polarimetric properties, it was shown that direct heating of the skin sample with a focused light beam reproducing the same spot size of the plasma jet and the same steady-state temperature of the irradiated area, results in the same modifications of linear retardance and depolarization.

In addition, the observed changes in polarimetric parameters are not due to local dehydration of the skin samples. Indeed, the small water loss shown in Fig. 3 results in only a slight increase in LR, as shown in Fig. 4. At the same time, the increase in plasma jet power and treatment time results in a significant decrease in LR in the center of the treated area. Thus, although the effect of plasma on skin samples is primarily due to heating, it is unlikely to be due to water loss from skin tissue.

Finally, plasma-generated RONS have many effects in vivo on skin tissue, but contact with a droplet of 0.02%v H_2O_2 solution showed no detectable effect on Muller matrix parameters of the skin model in this study. This lack of effect was observed on non-living tissue over a time scale of 30 minutes. In the present work, the skin samples were defrosted and not placed in culture medium. Thus, the results obtained are not in contradiction with the numerous previous publications showing that plasma-produced RONS have numerous biological effects in-vivo and in-vitro. Furthermore, the concentration of H_2O_2 in the droplets is low and corresponds to the amount of the same molecules produced by an equivalent plasma treatment on a liquid surface. It is possible that a higher concentration of H_2O_2 will lead to skin modifications.

5. Conclusion

In this article, Mueller Polarimetric Imaging is used to analyzed effects of Non-Thermal Plasma 10~30 min after treatment of defrost pig skin samples. The aim is to show how MPI can be used to evidence skin microstructure modifications caused by NTP treatment. NTP power and treatment durations have been varied. In addition, heat treatment and H_2O_2 treatment have been performed to identify key parameters responsible of skin microstructure modifications.

1) MPI parameters such as Linear Retardance and Depolarization of the treated skin area are modified depending upon the plasma power. Under mild NTP conditions and temperature of 35°C, MPI parameters are not modified. Modifications appear from 45°C (0.5 W) and increase continuously up to 73°C (1.5 W).

2) Part of these modifications may be attributed to the heating of the skin sample and denaturation of collagen fibers.

3) Conversely, chemical treatment using H_2O_2, does not show any effect on polarimetric properties. On inert skin samples, such a small quantity of chemical species does not likely induce any change in the skin microstructure.

Mueller polarimetric imaging could be a breakthrough technology for the non-invasive and real-time investigation of the structural modifications of the skin occurring in the development and treatment of pathologies such as skin cancers, blood coagulation wounds, and burns. RONS are considered to play an essential role in many biomedical processes such as the production extracellular matrix or angiogenesis. As a next step, instead of defrost inert skin, MPI could also be used to monitor the effect of NTP treatments on tissue metabolism and production of collagen in living tissues in *in-vivo* or *ex-vivo* studies.

Disclosures. The authors declare no conflicts of interest.

Data availability. Data underlying the results presented in this paper are not publicly available at this time but may be obtained from the authors upon reasonable request.

Supplemental document. See Supplement 1 for supporting content.

References

1. I. Adamovich, S. D. Baalrud, and A. Bogaerts, *et al.*, "The 2017 Plasma Roadmap: low temperature plasma science and technology," J. Phys. D: Appl. Phys. **50**(32), 323001 (2017).
2. D. B. Graves, "Reactive species from cold atmospheric plasma: implications for cancer therapy," Plasma Process. Polym. **11**(12), 1120–1127 (2014).
3. B. Haertel, T. von Woedtke, K.-D. Weltmann, and U. Lindequist, "Non-thermal atmospheric-pressure plasma possible application in wound healing," Biomol. Ther. **22**(6), 477–490 (2014).
4. C. Duchesne, N. Frescaline, J.-J. Lataillade, and A. Rousseau, "Comparative study between direct and indirect treatment with cold atmospheric plasma on *in vitro* and *in vivo* models of wound healing," PMED **8**(4), 379–401 (2018).
5. C. Duchesne, S. Banzet, J.-J. Lataillade, A. Rousseau, and N. Frescaline, "Cold atmospheric plasma modulates endothelial nitric oxide synthase signalling and enhances burn wound neovascularisation," J. Pathol. **249**(3), 368–380 (2019).
6. K. Wende, S. Straßenburg, B. Haertel, M. Harms, S. Holtz, A. Barton, K. Masur, T. von Woedtke, and U. Lindequist, "Atmospheric pressure plasma jet treatment evokes transient oxidative stress in HaCaT keratinocytes and influences cell physiology," Cell Biol. Int. **38**(4), 412–425 (2014).
7. J. Heinlin, G. Isbary, W. Stolz, G. Morfill, M. Landthaler, T. Shimizu, B. Steffes, T. Nosenko, J. Zimmermann, and S. Karrer, "Plasma applications in medicine with a special focus on dermatology," Journal of the European Academy of Dermatology and Venereology **25**(1), 1–11 (2011).

8. J.-H. Choi, Y.-S. Song, H.-J. Lee, J.-W. Hong, and G.-C. Kim, "Inhibition of inflammatory reactions in 2,4-Dinitrochlorobenzene induced Nc/Nga atopic dermatitis mice by non-thermal plasma," Sci. Rep. **6**(1), 27376 (2016).

9. G. Isbary, J. Heinlin, T. Shimizu, J. l. Zimmermann, G. Morfill, H.-U. Schmidt, R. Monetti, B. Steffes, W. Bunk, Y. Li, T. Klaempfl, S. Karrer, M. Landthaler, and W. Stolz, "Successful and safe use of 2 min cold atmospheric argon plasma in chronic wounds: results of a randomized controlled trial," Br. J. Dermatol. **167**(2), 404–410 (2012).

10. A. Schmidt, S. Bekeschus, K. Wende, B. Vollmar, and T. von Woedtke, "A cold plasma jet accelerates wound healing in a murine model of full-thickness skin wounds," Exp. Dermatol. **26**(2), 156–162 (2017).

11. S. Arndt, P. Unger, M. Berneburg, A.-K. Bosserhoff, and S. Karrer, "Cold atmospheric plasma (CAP) activates angiogenesis-related molecules in skin keratinocytes, fibroblasts and endothelial cells and improves wound angiogenesis in an autocrine and paracrine mode," J. Dermatol. Sci. **89**(2), 181–190 (2018).

12. S. Mashayekh, H. Rajaee, M. Akhlaghi, B. Shokri, and Z. M. Hassan, "Atmospheric-pressure plasma jet characterization and applications on melanoma cancer treatment (B/16-F10)," Phys. Plasmas **22**(9), 093508 (2015).

13. M. Dezest, L. Chavatte, M. Bourdens, D. Quinton, M. Camus, L. Garrigues, P. Descargues, S. Arbault, O. Burlet-Schiltz, L. Casteilla, F. Clément, V. Planat, and A.-L. Bulteau, "Mechanistic insights into the impact of cold atmospheric pressure plasma on human epithelial cell lines," Sci. Rep. **7**(1), 41163 (2017).

14. C.-J. Lin, T.-L. Chen, Y.-Y. Tseng, G.-J. Wu, M.-H. Hsieh, Y.-W. Lin, and R.-M. Chen, "Honokiol induces autophagic cell death in malignant glioma through reactive oxygen species-mediated regulation of the p53/PI3K/Akt/mTOR signaling pathway," Toxicol. Appl. Pharmacol. **304**, 59–69 (2016).

15. G. Fridman, M. Peddinghaus, M. Balasubramanian, H. Ayan, A. Fridman, A. Gutsol, and A. Brooks, "Blood coagulation and living tissue sterilization by floating-electrode dielectric barrier discharge in air," Plasma Chem. Plasma Process. **26**(4), 425–442 (2006).

16. G. D. Masi, C. Gareri, L. Cordaro, A. Fassina, P. Brun, B. Zaniol, R. Cavazzana, E. Martines, M. Zuin, G. Marinaro, S. D. Rosa, and C. Lndolfi, "Plasma coagulation controller: a low- power atmospheric plasma source for accelerated blood coagulation," Plasma Medicine **8**(3), 245 (2018).

17. A. Duval, I. Marinov, G. Bousquet, G. Gapihan, S. M. Starikovskaia, A. Rousseau, and A. Janin, "Cell death induced on cell cultures and nude mouse skin by non-thermal, nanosecond-pulsed generated plasma," PLoS One **8**(12), e83001 (2013).

18. L. Cordaro, G. De Masi, A. Fassina, D. Mancini, R. Cavazzana, D. Desideri, P. Sonato, M. Zuin, B. Zaniol, and E. Martines, "On the electrical and optical features of the plasma coagulation controller low temperature atmospheric plasma jet," Plasma **2**(2), 156–167 (2019).

19. N. Chernets, J. Zhang, M. J. Steinbeck, D. S. Kurpad, E. Koyama, G. Friedman, and T. A. Freeman, "Nonthermal atmospheric pressure plasma enhances mouse limb bud survival, growth, and elongation," Tissue Eng., Part A **21**(1-2), 300–309 (2015).

20. A. Mora-Núñez, G. Martínez-Ponce, G. García-Torales, and A. B. Beltrán-González, "Texture analysis applied to polarimetric images of healthy in vivo murine skin," Opt. Eng. **57**(05), 1 (2018).

21. A. Pierangelo, S. Manhas, A. Benali, C. Fallet, M.-R. Antonelli, T. Novikova, B. Gayet, P. Validire, and A. D. Martino, "Ex vivo photometric and polarimetric multilayer characterization of human healthy colon by multispectral Mueller imaging," J. Biomed. Opt **17**(6), 066009 (2012).

22. A. Pierangelo, A. Nazac, A. Benali, P. Validire, H. Cohen, T. Novikova, B. H. Ibrahim, S. Manhas, C. Fallet, M.-R. Antonelli, and A.-D. Martino, "Polarimetric imaging of uterine cervix: a case study," Opt. Express **21**(12), 14120–14130 (2013).

23. J. Rehbinder, H. Haddad, S. Deby, B. Teig, A. Nazac, T. Novikova, A. Pierangelo, and F. Moreau, "Ex vivo Mueller polarimetric imaging of the uterine cervix: a first statistical evaluation," J. Biomed. Opt **21**(7), 071113 (2016).

24. J. Vizet, J. Rehbinder, S. Deby, S. Roussel, A. Nazac, R. Soufan, C. Genestie, C. Haie-Meder, H. Fernandez, F. Moreau, and A. Pierangelo, "In vivo imaging of uterine cervix with a Mueller polarimetric colposcope," Sci. Rep. **7**(1), 2471 (2017).

25. M. Kupinski, M. Boffety, F. Goudail, R. Ossikovski, A. Pierangelo, J. Rehbinder, J. Vizet, and T. Novikova, "Polarimetric measurement utility for pre-cancer detection from uterine cervix specimens," Biomed. Opt. Express **9**(11), 5691–5702 (2018).

26. C. Heinrich, J. Rehbinder, A. Nazac, B. Teig, A. Pierangelo, and J. Zallat, "Mueller polarimetric imaging of biological tissues: classification in a decision-theoretic framework," J. Opt. Soc. Am. A **35**(12), 2046–2057 (2018).

27. T. Novikova, A. Pierangelo, A. De Martino, A. Benali, and P. Validire, "Polarimetric Imaging for Cancer Diagnosis and Staging," Opt. Photonics News **23**(10), 26 (2012).

28. A. Pierangelo, A. Benali, M.-R. Antonelli, T. Novikova, P. Validire, B. Gayet, and A. D. Martino, "Ex-vivo characterization of human colon cancer by Mueller polarimetric imaging," Opt. Express **19**(2), 1582–1593 (2011).

29. M.-R. Antonelli, A. Pierangelo, T. Novikova, P. Validire, A. Benali, B. Gayet, and A. D. Martino, "Mueller matrix imaging of human colon tissue for cancer diagnostics: how Monte Carlo modeling can help in the interpretation of experimental data," Opt. Express **18**(10), 10200–10208 (2010).

30. A. Pierangelo, S. Manhas, A. Benali, C. Fallet, J.-L. Totobenazara, M. R. Antonelli, T. Novikova, B. Gayet, A. D. Martino, and P. Validire, "Multispectral Mueller polarimetric imaging detecting residual cancer and cancer regression after neoadjuvant treatment for colorectal carcinomas," J. Biomed. Opt **18**(4), 046014 (2013).

31. W. Wang, L. G. Lim, S. Srivastava, J. Bok-Yan So, A. Shabbir, and Q. Liu, "Investigation on the potential of Mueller matrix imaging for digital staining," J. Biophoton **9**(4), 364–375 (2016).

32. M. H. Smith, P. D. Burke, A. Lompado, E. A. Tanner, and L. W. Hillman, "Mueller matrix imaging polarimetry in dermatology," in *Biomedical Diagnostic, Guidance, and Surgical-Assist Systems II* (SPIE, 2000), 3911, pp. 210–216.

33. M. H. Smith, "Interpreting Mueller matrix images of tissues," in *Laser-Tissue Interaction XII: Photochemical, Photothermal, and Photomechanical* (SPIE, 2001), 4257, pp. 82–89.

34. Y. Dong, H. He, W. Sheng, J. Wu, and H. Ma, "A quantitative and non-contact technique to characterise microstructural variations of skin tissues during photo-damaging process based on Mueller matrix polarimetry," Sci Rep **7**(1), 14702 (2017).

35. J. Vizet, S. Manhas, J. Tran, P. Validire, A. Benali, E. Garcia-Caurel, A. Pierangelo, A. D. Martino, and D. Pagnoux, "Optical fiber-based full Mueller polarimeter for endoscopic imaging using a two-wavelength simultaneous measurement method," J. Biomed. Opt **21**(7), 071106 (2016).

36. J. Fade and M. Alouini, "Depolarization remote sensing by orthogonality breaking," Phys. Rev. Lett. **109**(4), 043901 (2012).

37. Y. Gorbanev, D. O'Connell, and V. Chechik, "Non-thermal plasma in contact with water: The origin of species," Chem. Eur. J. **22**(10), 3496–3505 (2016).

38. O. Chashchina, H. Mezouar, J. Vizet, C. Raoux, J. Park, C. Ramón-Lozano, M.-C. Schanne-Klein, A. I. Barakat, and A. Pierangelo, "Mueller polarimetric imaging for fast macroscopic mapping of microscopic collagen matrix remodeling by smooth muscle cells," Sci. Rep. **11**(1), 5901 (2021).

39. E. Compain, S. Poirier, and B. Drevillon, "General and self-consistent method for the calibration of polarization modulators, polarimeters, and Mueller-matrix ellipsometers," Appl. Opt. **38**(16), 3490–3502 (1999).

40. A. Lindberg, J. Vizet, J. Rehbinder, C. Gennet, J.-C. Vanel, and A. Pierangelo, "Innovative integrated numerical-experimental method for high-performance multispectral Mueller polarimeters based on ferroelectric liquid crystals," Appl. Opt. **58**(19), 5187–5199 (2019).

41. A. Lindberg, J. Vizet, J. Rehbinder, C. Gennet, J.-C. Vanel, and A. Pierangelo, "Innovative and high-performance instrumentation for biomedical Mueller polarimetric imaging in vivo," in *Optical Biopsy XVII: Toward Real-Time Spectroscopic Imaging and Diagnosis* (SPIE, 2019), 10873, pp. 28–35.

42. S.-Y. Lu and R. A. Chipman, "Interpretation of Mueller matrices based on polar decomposition," J. Opt. Soc. Am. A **13**(5), 1106–1113 (1996).

43. D. A. Hirth, A. J. Singer, R. A. F. Clark, and S. A. McClain, "Histopathologic staining of low temperature cutaneous burns: comparing biomarkers of epithelial and vascular injury reveals utility of HMGB1 and hematoxylin phloxine saffron," Wound Repair and Regeneration **20**(6), 918–927 (2012).

44. M. Singh, K. Nuutila, R. Minasian, C. Kruse, and E. Eriksson, "Development of a precise experimental burn model," Burns **42**(7), 1507–1512 (2016).

45. B. Baumann, D. J. Harper, P. Eugui, J. Gesperger, A. Lichtenegger, C. W. Merkle, M. Augustin, and A. Woehrer, "Improved accuracy of quantitative birefringence imaging by polarization sensitive OCT with simple noise correction and its application to neuroimaging," J. Biophotonics **14**(4), e202000323 (2021).

46. C. J. Liu, W. Ammon, R. J. Jones, J. Nolan, R. Wang, S. Chang, M. P. Frosch, A. Yendiki, D. A. Boas, C. Magnain, B. Fischl, and H. Wang, "Refractive-index matching enhanced polarization sensitive optical coherence tomography quantification in human brain tissue," Biomed. Opt. Express **13**(1), 358–372 (2022).